ARTICLE OPEN

Check for updates

Hole-doping induced ferromagnetism in 2D materials

Ruishen Meng [1 ✉], Lino da Costa Pereira[1], Jean-Pierre Locquet [1], Valeri Afanas'ev [1], Geoffrey Pourtois [2] and Michel Houssa[1,2 ✉]

Two-dimensional (2D) ferromagnetic materials are considered as promising candidates for the future generations of spintronic devices. Yet, 2D materials with intrinsic ferromagnetism are scarce. Hereby, high-throughput first-principles simulations are performed to screen 2D materials that present a non-magnetic to a ferromagnetic transition upon hole doping. A global evolutionary search is subsequently performed to identify alternative possible atomic structures of the eligible candidates, and 122 materials exhibiting a hole-doping induced ferromagnetism are identified. Their energetic and dynamic stability, as well as magnetic properties under hole doping are investigated systematically. Half of these 2D materials are metal halides, followed by chalcogenides, oxides, and nitrides, some of them having predicted Curie temperatures above 300 K. The exchange interactions responsible for the ferromagnetic order are also discussed. This work not only provides theoretical insights into hole-doped 2D ferromagnetic materials, but also enriches the family of 2D magnetic materials for possible spintronic applications.

INTRODUCTION

Magnetic materials, especially ferromagnetic semiconductors, are considered advantageous in the field of spintronics because of their easy integration into semiconductor devices[1–3]. Apart from the intrinsic magnetic materials, research attention has also been focusing on dilute magnetic semiconductors (DMSs), where the magnetism is induced by $3d^n$ transition metal ions doping[4,5]. One of the representative examples is the Mn-doped GaAs[6], which shows spontaneous magnetization up to 110 K. In addition, the so-called 'd^0' ferromagnetic materials[7] that contain no partially filled d or f bands, have also developed into an important branch of magnetic materials. The ferromagnetism in a series of these 'd^0' ferromagnetic materials was observed even above room temperature[8–11]. Hole mediation is considered to be the origin of the 'd^0 ferromagnetism', which can be realized by acceptor doping or even by intrinsic defects[12–14]. This 'd^0 ferromagnetism' offers a different way and possibility to hunt for high-temperature spintronic materials.

The past decade has witnessed the rapid development of the 2D magnetic materials[15–18]. In particular, the study of van der Waals (vdW) layered 2D CrI₃, Cr₂Ge₂Te₆, Fe₃GeTe₂, VSe₂, etc. has sparked intense research interests in the field of 2D magnetism[19–23]. The absence of dangling bonds, the possibility of layer-by-layer control of the thickness and the magnetic properties, together with the construction of artificial heterostructures, without the need for lattice matching of these vdW 2D materials, are making them promising candidates for the next-generation spintronic devices[24,25]. For instance, 2D CrI₃ used as a spin-filter tunnel barrier sandwiched between graphene contacts can have ultra-high tunneling magnetoresistance of 19,000%[26]. However, the scarcity of 2D ferromagnetic semiconductors/half-metals and their rather low Curie temperature (T_c) may hamper practical applications as well as the further investigation of 2D magnetism. Continuous seeking for more 2D ferromagnetic semiconducting or half-metallic materials with relatively high Curie temperature is necessary. On the other hand, 2D diluted magnetic semiconductors (2D DMSs) have also attracted much research interests, as their electronic and magnetic properties can be tuned by changing the dopant type as well as the doping concentration. Although 2D DMSs could encounter some issues, such as magnetic dopant clustering with an increase in doping concentration, as well as a low saturation magnetization, few 2D transition metal dichalcogenide-based DMSs were predicted to be suitable candidates for realizing room-temperature ferromagnetism[27,28], as also confirmed by recent experimental works[29,30].

Similar to the bulk 'd^0' ferromagnetic materials, researches have predicted that the 2D III-VI (gallium oxides/chalcogenides and indium oxides/chalcogenides)[31–35] and IV–VI (tin oxides/chalcogenides and lead oxides)[36–38] semiconductors, and some other 2D materials such as InP₃, etc[39–42]. would exhibit non-magnetic to ferromagnetic, and semiconducting to half-metallic transition upon hole doping. Ferromagnetism in these hole-doped 2D materials arises from an exchange splitting of electronic states at the top of the valence band, where the density of states (DOS) exhibits a sharp Van Hove singularity, that would lead to an electronic instability. The magnetic moments of these hole-doped 2D ferromagnetic materials are mainly contributed by the delocalized p orbitals of the anions, which could be advantageous for the long-range ferromagnetic order. However, a systematic investigation of the magnetic properties of these 2D materials (spin-polarization energies, magnetic exchange coupling strength, magnetic anisotropy, and Curie temperature) is lacking. Besides, the mechanism responsible for the exchange coupling and delocalization of the spin-polarized holes has not been discussed, to our knowledge. In addition, it is also of significance to find out whether there are other 2D materials which become ferromagnetic upon hole doping.

Using these hole-mediated ferromagnetic 2D materials in spin-polarized field-effect devices, it should be possible to control their magnetic state by means of a gate bias, which could be very interesting in e.g. magnetic tunnel junctions (MTJ). As a matter of fact, the injection of spin-polarized carriers in such devices, controlled by a gate bias, should be much more energetically efficient (reduced power consumptions) as compared to MTJ using spin-torque effects, where the injection of large spin-polarized currents is necessary. Note that high doping carrier

[1]Department of Physics and Astronomy, KU Leuven, Celestijnenlaan 200D, Leuven B-3001, Belgium. [2]imec, Kapeldreef 75, B-3001 Leuven, Belgium.
✉email: ruishen.meng@kuleuven.be; michel.houssa@kuleuven.be

densities of the order of $10^{14}\,cm^{-2}$ have been achieved in 2D materials by electrolyte gating[43–45]. Non-magnetic acceptor impurities or intrinsic defects can also lead to the hole-doping of these 2D materials, facilitating the transition from the non-magnetic to ferromagnetic state.

In this study, we screen thousands of 2D non-magnetic semiconductors/insulators from three databases[46–48], followed by a high-throughput density functional theory calculation to identify potential 2D ferromagnetic materials induced by hole doping. We then verify the stability of the potential candidates with respect to competing atomic structures, obtained by global structure searching based on evolutionary algorithm[49], via exploring energy convex hulls and phonon spectrum. Afterwards, the magnetic behaviors of the stable candidates at different doping densities are investigated systematically. Eventually, 122 materials are recognized as stable 2D ferromagnetic materials upon hole doping, some of them having a computed Curie temperature near or above room temperature. The exchange interaction mechanisms responsible for the ferromagnetic coupling in these 2D materials are also discussed.

RESULTS AND DISCUSSION
High-throughput screening process
The general workflow of this research is illustrated by a funnel plot on the left panel of Fig. 1, which is categorized into five processes; the number of materials used for screening and the screening criteria in each process is also given. As a starting point, to include as many 2D materials as possible, we gather about 8000 2D crystal structures from three databases, 2DMatPedia[48], computational 2D materials database (C2DB)[46] and Materials Cloud two-dimensional crystals database (MC2D)[47] that contains exfoliable 2D materials. In the prescreening process, the magnetic as well as the metallic materials are excluded since we are only interested in the non-magnetic semiconductors. Besides, the repeated structures and the structures with low thermodynamic stability ($E_c > 0.2$ eV per

atom, E_c is the cohesive energy defined by the total energy of the compound minus the total energies of its constituent atoms) are also screened out. As a result, about 3000 non-magnetic 2D semiconducting materials, with moderate stability, are picked out for the subsequent hole doping simulations.

The typical doping densities, ranging from $5 \times 10^{12}\,cm^{-2}$ to $8 \times 10^{14}\,cm^{-2}$ are used in the hole doping simulations, and structural relaxations are carried out for each doping density. The spin-polarization energy is obtained by $E_{spin} = E_{NM} - E_{FM}$, where E_{FM} and E_{NM} are the energy of the ferromagnetic and non-magnetic states, respectively at PBE level. In this case, a positive E_{spin} suggests that the ferromagnetic state is more energetically stable. Typically, for the GaS, GaSe and InSe monolayer, the maximum E_{spin} is about 10 meV per hole[31,32,35], whereas other materials, like GaO, SnO, etc.[34,37] have relatively larger E_{spin}. Herein, we use this 10 meV per hole as a standard value, and materials with E_{spin} smaller than 10 mev per hole are discarded. The induced magnetic moment is also compared with the number of holes used in the simulation. If the ratio of magnetic moment to hole number is ~1 (1 μ_B per hole), it indicates that the injected holes can be fully spin polarized. Materials with induced magnetic moment much smaller than 1 μ_B per hole are excluded. Finally, materials exhibiting ferromagnetism only at a hole density below $10^{13}\,cm^{-2}$ or only after a high hole density of $6 \times 10^{14}\,cm^{-2}$ are also discarded.

A globally evolutionary structure searching is subsequently carried out to explore atomic structures with different stoichiometries, for a given material that shows promising ferromagnetic properties upon hole doping. In this step, the formation enthalpy as a function of the composition ratio for the atomic structures found in the searching process is provided. Structures with formation enthalpy on the convex hull are considered to be thermodynamically stable. If a new structure/phase on the convex hull is found, it is sent back to the hole doping simulations. Subsequently, the number of candidate materials is narrowed down to 736. According to their chemical formula, these
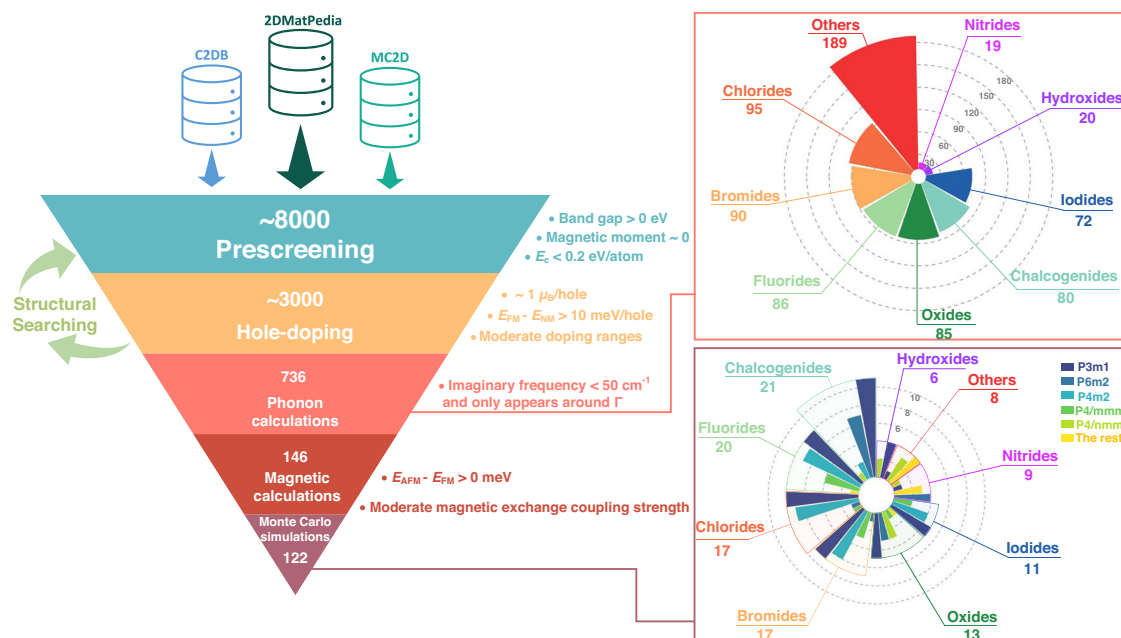

Fig. 1 The workflow of the high-throughput screening for 2D hole-doping induced ferromagnetic materials. 2D structures are collected from 2DMatpedia Database, Computational 2D Materials Database (C2DB) and Materials Cloud two-dimensional crystals database (MC2D) to identify potential 2D ferromagnetic materials upon hole doping (left panel). The number of candidate materials and the screening criteria used for each screening step are provided. Polar histogram showing the number of structures belonging to different chemical compositions after hole doping screening (top right panel); Polar histogram displaying the number of final stable 2D ferromagnetic materials in terms of chemical compositions and their crystal space groups (bottom right panel).

candidate materials are classified into different prototypes, as shown by the polar histogram on the top right panel of Fig. 1. The most prevalent chemical composition corresponds to metal halides (~47%), followed by other materials such as ternary compounds, phosphorides, carbides, etc. (~26%, grouped as 'Others'). Oxides (~12%) and chalcogenides (~11%) also account for a part of the candidate materials. There is also a fraction of hydroxides (~3%) and nitrides (~3%). Phonons calculations on these candidates are next performed, to verify their dynamic stability. In this procedure, materials with imaginary frequency only appears around the Γ point in the first Brillouin zone and less than 50 cm^{-1} are regarded as dynamically stable. Afterwards, 146 candidates are selected for further screening.

The next step consists in performing detailed calculations of the magnetic properties of these selected 2D materials, i.e., magnetic exchange coupling strength, magnetic anisotropy energy (MAE), and Curie temperature. Generally, the magnetic moments of 2D hole-doped ferromagnetic materials are well localized on the p-orbitals of the anion sites, which is also confirmed by the HSE06 calculations in Supplementary Fig. 1 that the spin density localized

almost solely on the anion site. Therefore, their FM configuration as well as a few antiferromagnetic (AFM) configurations can be constructed and it is valid to map their energies obtained from first-principles calculations to the Heisenberg spin Hamiltonian:

$$H = -\sum_{i \neq j} J_{ij} S_i \cdot S_j - A \sum_i (S_i^z)^2 \qquad (1)$$

where J_{ij} is the exchange interaction between i and j atomic sites, S_i is a unit vector denoting the local spin direction of atom i, and S_j is the unit vector of the spin moment direction of atom j. For ferromagnetic materials where neighboring spins align in parallel, $J_{ij} > 0$, while for antiferromagnetic materials where the spins prefer to align anti-parallel, $J_{ij} < 0$. A is the MAE per magnetic ion, where positive values correspond to a preferred alignment along the z-axis, while negative values correspond to a preferred alignment along the $x - y$ plane. The J_{ij} can then be obtained by comparing the total energies of different magnetic configurations[50,51]. Materials with negative magnetic exchange couplings, i.e., whose antiferromagnetic state is more energetically stable than the ferromagnetic one, or materials with weak FM coupling ($J_{ij} <$ meV)
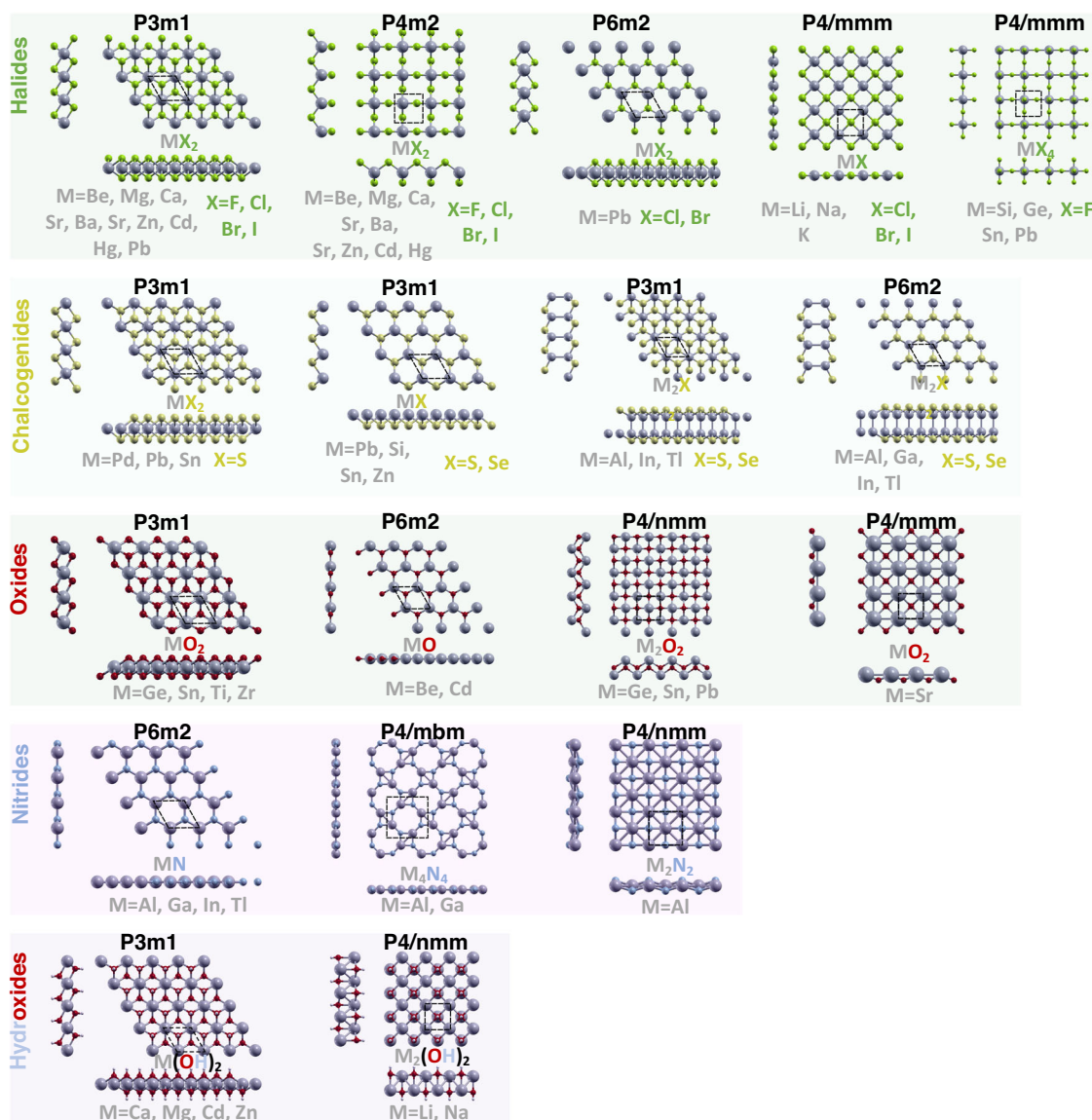

Fig. 2 Overview of the representative atomic structures of the 2DHDFM, sorted by chemical compositions and space groups. The chemical formula and the corresponding constituent elements of each atomic structures are provided, and the unit cells are marked out by the black dotted lines.
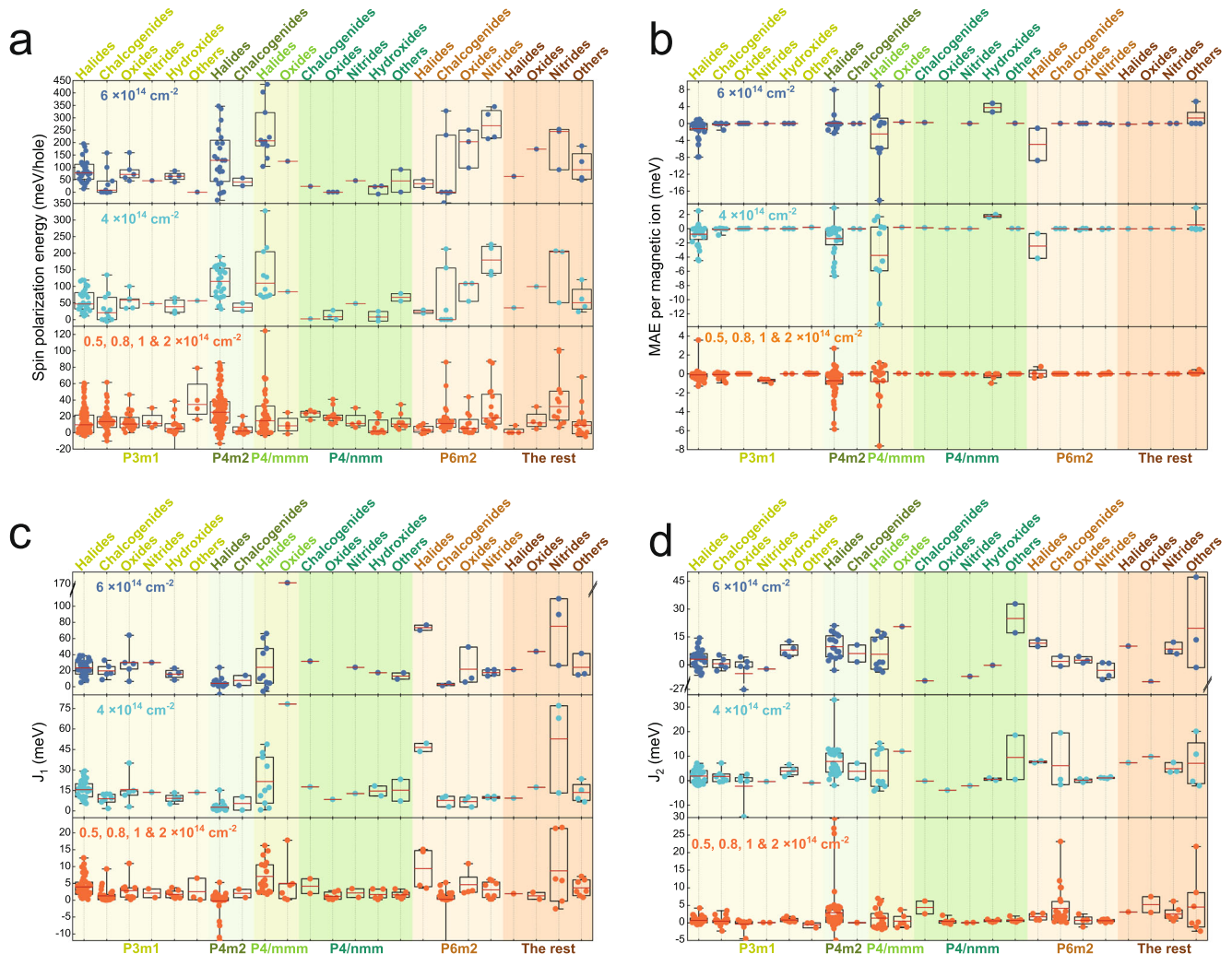
Fig. 3 Distribution of spin-polarization energies, magnetic anisotropic energies (MAE) per magnetic ion and magnetic exchange interaction parameters of the 2DHDFM. Box plots of the spin-polarization energies (**a**) magnetic anisotropic energies (MAE) per magnetic ion (**b**) nearest-neighbor exchange interaction parameters, J_1 (**c**) and next-nearest-neighbor exchange interaction parameters J_2 (**d**) at specific hole doping density of the 122 2DHDFM, classified by space group and chemical composition. The box plots show the extrema (whisker tails), interquartile range (box boundaries), and median (red horizontal line).

are not considered further. In our high-throughput calculations, only the isotropic (scalar) form of J_{ij} is used to reduce the simplicity of computation and comparison. It should be noted that, dependent on the spin-orbit interaction, the J_{ij} can be anisotropic (i.e. represented by a tensor), and this can affect the estimated Curie temperatures to some extent[52,53].

Through the screening process described above, 122 candidates are identified as stable 2D hole-doped ferromagnetic materials upon hole doping, which are denoted as 2DHDFM hereafter. These materials become half-metals after hole doping, with a metallic DOS at the Fermi level (E_F) for the spin-down channels and a simultaneous band gap for the spin-up channels. The magnetic moment of 2DHDFM is primarily originating from the p-orbitals of the anions. In the following, we focus on the analysis of their structural and magnetic properties. More detailed information, including their formation energies in the convex hull, atomic structures and atomic coordinates, phonon dispersion spectra, band structures and electronic density of states, magnetic moment and spin polarization energy as a function of hole density, magnetic configurations and the corresponding spin Hamiltonian, the magnetic exchange coupling strength, MAE and temperature-dependent normalized magnetization curves at specific hole density are provided in the supplementary materials.

Chemical compositions and structural properties of 2DHDFM

The classification of 2DHDFM based on their chemical composition and space group is shown by the polar histogram on the bottom right panel of Fig. 1. Clearly, 65 out of 122 candidates belong to metal halides, including 20 fluorides, 17 chlorides, 17 bromides and 11 iodides. The rest covers 21 chalcogenides, 13 oxides, 9 nitrides, 6 hydroxides and 8 other materials. Among those materials, P3m1 is the primary space group, followed by the P4m2 and P6m2. The representative atomic structures of these materials in different space groups are given in Fig. 2.

The metal elements in the 2D dihalides with P3m1 and P4m2 space groups are mainly from the group IIA Be, Mg, Ca, Sr and Ba, and group IIB Zn Cd and Hg. The atomic structure of the P3m1-dihalides is commonly known as the 1 T structure, with one halogen atom bonded to three neighboring metal atoms. The ones with P4m2 space group have a tetragonal lattice with one halogen atom connecting to only two neighboring metal atoms. According to their convex hulls, P3m1-dihalides are usually more stable than the P4m2-ones, except for $ZnBr_2$. $PbCl_2$ and $PbBr_2$ are the only two halides with P6m2 space group, and their structure is commonly known as the 2H hexagonal structure. Nevertheless, they are less stable than the P3m1 counterparts. In addition, there

are two different halide structures with tetragonal P4/mmm space group. They contain metal elements from group IA and group IVA, respectively. The former form metal monohalides, such as LiCl and NaBr, with both halogen and metal atoms being fourfold coordinated. The latter consist in tetrahalides, AF_4 (A = Si, Ge, Sn, Pb), with an atomic structure similar to the P4m2 dihalides, the two extra fluorine atoms forming bonds to one A atom along the out-of-plane direction in the unit-cell.

The majority of chalcogenides belongs to the P3m1 and P6m2 space groups, while a few of them belong to the P4m2 and P4/mmm space groups. The chalcogenides mainly consist of elements from the group IIIA Al, Ga, In, Tl, group IVA Si, Sn, Pb and group IIB Zn and Cd. The monochalcogenides, MX (M = Al, Ga, In, Tl; X = S, Se), which contain two metal atoms and two chalcogenide atoms in the unit cell, have both P3m1 and P6m2 space groups. Each X atom is bonded to three neighboring M atoms, and every M atom is fourfold coordinated, forming bonds with three adjacent X atoms and one M atom, with a characteristic X-M-M-X vertical stacking. The only difference between the two space groups is that the X atoms in the upper and bottom layer overlap with each other from the top view of the atomic plane for the P6m2 structures, while they have stagger position in the P3m1 structures. For a given material, the total energy difference between these two space groups is very small (typically less than 50 meV per unit cell). Note that these monochalcogenides gradually become non-magnetic when the hole doping density is typically larger than $2 \times 10^{14} cm^{-2}$. There are two other P3m1 atomic structures for the chalcogenides. The first one corresponds to the dichalcogenides, including SnS_2, PbS_2 and PdS_2, having the 1 T hexagonal structure. The second one corresponds to the monochalcogenides SiS, SnS, PbS, PbSe and ZnSe, holding the buckled hexagonal structure. The space group of CdS and ZnS, however, belongs to P6m2, because of the planar hexagonal atomic plane.

Concerning the 2DHDFM oxides, GeO_2, SnO_2, TiO_2 and ZrO_2 belong to the P3m1 space group with 1 T structure, while the space group of BeO, CdO is P6m2 (similar to CdS and ZnS), with their atomic planes being also planar. Another space group of the oxides is P4/nmm, which includes GeO, SnO and PbO. In these three materials, each cation (anion) is bonded to four neighboring anions (cations) in the tetragonal structure. SrO_2 is the only oxide with P4/mmm space group, and each O atom bonds to four neighboring Sr atoms, while each Sr atom bonds to eight O atoms.

AlN, GaN, InN and TlN are the four 2DHDFM nitrides with planar hexagonal P6m2 structure. The rest of the 2D nitrides include planar tetragonal Al_4N_4 and Ga_4N_4 with P4/mbm, two Al_2N_2 structures with either P3m1 or P4/nmm space group, and C_3N_4 with C2 space group. In addition, there are only six 2DHDFM hydroxides, including $Ca(OH)_2$, $Mg(OH)_2$, $Cd(OH)_2$ and $Zn(OH)_2$ with P3m1 space group, and $Li_2(OH)_2$, $Na_2(OH)_2$ with P4/nmm space group. The P3m1 and P4/nmm-hydroxides have structures similar to the 1 T structure, and the ones of GeO, SnO and PbO, respectively, with the two O atoms terminated by two H atoms in the unit cell. Note that these six hydroxides have all parent 3D bulk structures and can be easily exfoliated[47]. The remaining 2DHDFM mainly involve ternary compounds, such as $Pb_2Br_2F_2$, $Sc_2Br_2O_2$ and $Sr_2Br_2H_2$ with P4/nmm, $In_2Br_2O_2$ and $In_2Cl_2O_2$ with Pmmn, and $TiPbO_3$ with P4mm space group.

Spin polarization energies of 2DHDFM

The spin-polarization energies E_{spin} of 2DHDFM at different doping densities are presented in Fig. 3a. Generally, E_{spin} increases monotonically as the hole doping density increases. There is a clear distinction in the E_{spin} distribution among different compounds with different space groups. For the P3m1, P4m2 and P4/mmm space groups, halides typically have high median as well as large E_{spin} at a given hole doping density. Besides, the oxides and nitrides with P6m2 also have moderate to high E_{spin},

Table 1. Spin polarization energy E_{spin}, electronegativity difference $\Delta\chi$, magnetic anisotropic energy MAE, nearest-neighbor exchange interaction parameter J_1, next-nearest-neighbor exchange interaction parameter J_2, and Curie temperature T_c at hole doping density of $6 \times 10^{14} cm^{-2}$ for the P3m1-halides.

	E_{spin} (meV)	$\Delta\chi$	MAE (µeV)	J_1 (meV)	J_2 (meV)	T_c (K)
BeF_2	120	1.94	−9	21.440	−3.343	26
MgF_2	152	2.67	−15	28.624	−3.931)	63
$MgCl_2$	101	1.85	−163	34.845	3.081	224
CaF_2	184	2.98	−62	23.212	−1.996	70
$CaCl_2$	80	2.16	−11	36.036	−5.636	49
$CaBr_2$	40	1.96	−613	27.296	−1.552	104
CaI_2	14	1.66	−620	5.415	0.663	42
SrF_2	195	3.03	−125	16.900	−0.740	63
$SrCl_2$	118	2.21	−295	32.319	−4.562	83
$SrBr_2$	71	2.01	126	38.474	−2.717	126
SrI_2	35	1.71	−1956	9.024	3.092	107
BaF_2	96	3.09	946	38.685	7.868	337
$BaCl_2$	167	2.27	195	20.222	−0.710	90
$BaBr_2$	110	2.07	320	32.384	1.431	181
BaI_2	73	1.77	−1776	11.161	5.215	162
ZnF_2	76	2.33	314	14.890	4.560	155
$ZnCl_2$	65	1.51	−314	20.431	2.748	161
$ZnBr_2$	42	1.31	−3800	13.446	5.452	179
CdF_2	107	2.29	816	29.730	9.200	320
$CdCl_2$	114	1.47	−171	31.241	0.785	162
$CdBr_2$	78	1.27	−5005	20.870	3.980	190
CdI_2	37	0.97	−7917	8.155	4.530	141
HgF_2	71	1.98	−1316	23.307	12.027	333
$HgCl_2$	84	1.16	366	30.671	6.515	270
$HgBr_2$	77	0.96	−3391	27.471	6.280	264
HgI_2	52	0.66	−7939	12.72	5.672	185
$PbCl_2$	53	0.83	0	27.041	14.43	394
$PbBr_2$	23	0.63	−1013	18.215	11.75	301

with medians of ~200 to ~250 meV per hole at $6 \times 10^{14} cm^{-2}$. On the other hand, the 2DHDFM with P4/nmm space group have relatively small E_{spin}, typically less than 100 meV per hole at $6 \times 10^{14} cm^{-2}$.

E_{spin} has the tendency of being relatively larger for the binary compounds with lighter anions in the same crystal structure. This is in agreement with values reported in the literature[31,32,34,35] for the 2D gallium or indium oxides and chalcogenides, with E_{spin} following the order of GaO > GaS > GaSe, and InO > InS > InSe. From our calculations, we find that for halides with the same space group, fluorides or chlorides usually have the largest E_{spin}, followed by bromides and iodides at the same hole doping density. As can be seen from Table 1, MgF_2 has larger E_{spin} than $MgCl_2$, and for the calcium halides, their E_{spin} follow the order CaF_2 > $CaCl_2$ > $CaBr_2$ > CaI_2. A similar trend is also clear for the strontium, barium, cadmium and zinc halides. Note, however, that the fluorides of barium, cadmium and mercury do not follow the same trend, their E_{spin} being smaller than the ones of their chloride counterparts. In fact, for materials with a larger difference in electronegativity ($\Delta\chi$) between the anions and cations, one expects a larger coulomb interaction and thus a larger exchange splitting, and subsequently, a larger E_{spin}. This may explain why the metal halides have generally larger E_{spin}, since their $\Delta\chi$ is large. In particular, the P4/mmm-monohalides have the largest E_{spin}, because the group IA metals have small electronegativities, while the halides (especially
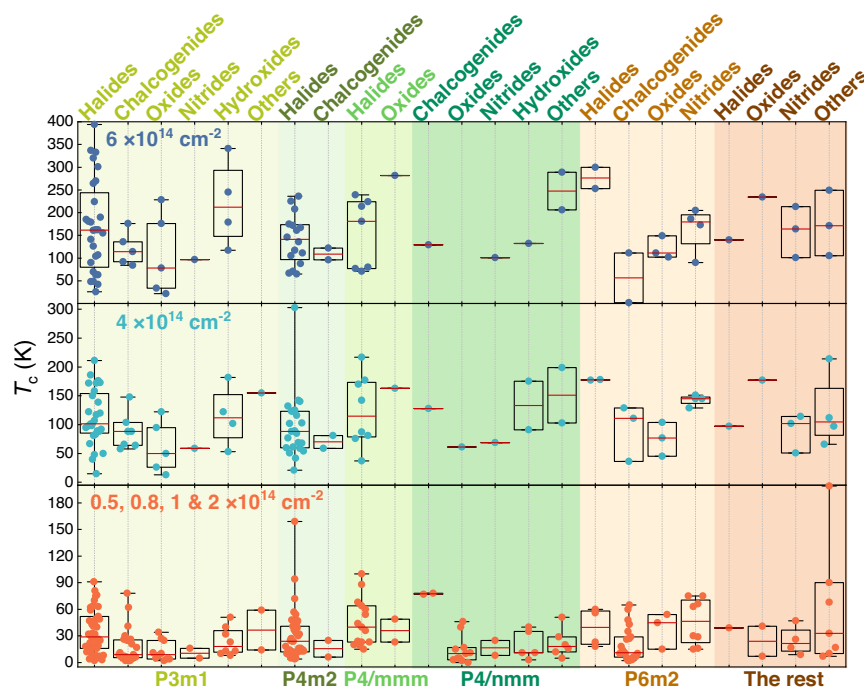
Fig. 4 Distribution of Curie temperatures of the 2DHDFM. Box plots of the Curie temperatures (T_c) obtained from Monte Carlo simulations for 2DHDFM at different hole doping densities. The red lines inside the boxes represent the median values and the horizontal bar denotes the low/high boundaries of the spreads. The box plots show the extrema (whisker tails), interquartile range (box boundaries), and median (red horizontal line).

fluoride) have large electronegativities. For instance, NaBr and KBr have quite high E_{spin}, over 400 meV per hole at 6×10^{14} cm^{-2}. The trend mentioned above for Ga and In oxides, sulfides, and selenides is also consistent with the decrease of the electronegativity from O to Se.

Magnetic anisotropy and magnetic exchange coupling of 2DHDFM

The magnetic anisotropy energy (MAE) of 2DHDFM varies from materials to materials, and generally grows as the hole doping density increases, as can be seen from Fig. 3b. The MAE of the majority of 2DHDFM are below 1 meV per magnetic ion. Particularly, metal halides have relatively large absolute MAE, as compared to other compounds, especially the ones with P4/mmm and P4m2 space groups. Some of them even have absolute MAE larger than 10 meV per magnetic ion at 4 and 6×10^{14} cm^{-2}. This is likely related to the large spin-orbit coupling strength of bromine and iodine. Other materials with lighter elements (and thus smaller spin-orbit coupling), like fluorides and oxides, have much smaller absolute MAE, usually less than 100 μeV per magnetic ion. Interestingly, the median of MAE of most 2DHDFM are negative, which reveals that the spins prefer to align along the in-plane direction.

The magnetic exchange coupling parameters of the 2DHDFM at different doping densities are summarized in Fig. 3c, d, where J_1 and J_2 represents the nearest and next-nearest neighbor coupling, respectively. These parameters can be obtained from the total energy difference of various possible ferromagnetic and antiferromagnetic configurations[50,51]. Overall, the magnetic exchange coupling parameters also increase by increasing the hole doping density. J_1 is positive for most 2DHDFM, which is characteristic of a ferromagnetic first-neighbor interaction. On the other hand, J_2 is typically smaller than J_1 (as expected), and J_2 is negative for a couple of 2DHDFM, suggesting competing ferromagnetic and antiferromagnetic interactions in these compounds, as discussed further below. The computed Curie temperature T_c of 2DHDFM is

summarized in Fig. 4. Increasing the hole doping density also gives rise to a higher T_c for most of 2DHDFM. Upon a hole doping density of 4×10^{14} cm^{-2}, the medians T_c of various 2DHDFM are in the range of ~50 K to ~170 K, and further increase to ~70 K to ~270 K at 6×10^{14} cm^{-2}. As expected, the Curie temperature is correlated to the values of the magnetic exchange coupling parameters. Very interestingly, the sign of J_2 is found to play a very important role on T_c. Consider the typical case of CaF$_2$ ($T_c = 70$ K) and HgF$_2$ ($T_c = 333$ K), which have the same P3m1 crystal structure (see Table 1). While these two materials have similar J_1 (about 23 meV), CaF$_2$ has a negative J_2 (about −2 meV) and HgF$_2$ has a positive J_2 (about 12 meV). A ferromagnetic next-nearest neighbor interaction thus favors a large T_c in these 2D materials, such as in BaF$_2$ (337 K), CdF$_2$ (320 K), HgF$_2$ (333 K), PbCl$_2$ (394 K) and PbBr$_2$ (301 K) at a hole doping density of 6×10^{14} cm^{-2}.

Discussion on the magnetic coupling mechanism

In general, the magnetic moments of 2DHDFM are mainly contributed by the anion p-orbitals, as shown in Fig. 5a. Since a large portion of these 2D materials consists of P3m1-dihalides, the magnetic properties of these materials are first discussed below. In these compounds, J_1 corresponds to the out-of-plane exchange coupling between two halogens from the top and bottom atomic planes, as shown in Fig. 6a; a local coordinate system is used for these P3m1-dihalides, where the metal ion is in the center of a distorted octahedra with six ligands at the vertices. Note that the shorter halogen-halogen distance is about 2.3 Å in fluorides, and gradually increases to about 5 Å from chlorides to iodides. Considering the delocalized nature of the p orbitals, the direct out-of-plane magnetic interaction mainly arises from the exchange coupling between the p_z orbitals of the halogens, as illustrated in Fig. 6b; this direct exchange coupling is ferromagnetic, leading to a positive value of J_1, which lies between about 5 and 39 meV (see Table 1). Note also that J_1 is smaller in iodides, due to the larger out-of-plane halogen-halogen distance in these compounds.
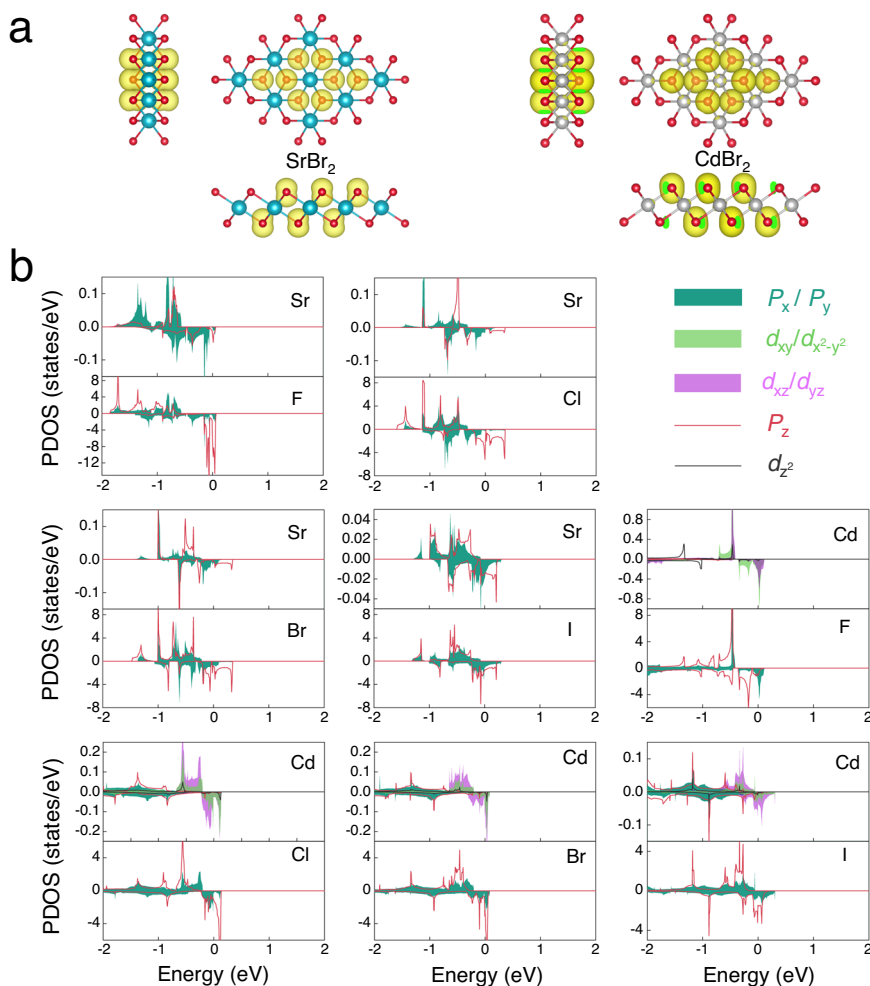
Fig. 5 Spin densities and orbital projected density of states of the selected 2DHDFM. Spin density plots (**a**) and orbital projected density of states (**b**) for P3m1 strontium dihalides and cadmium dihalides monolayers at hole density of 6×10^{14} cm^{-2}. Positive (negative) values refer to up (down) spins. The Fermi level is set at zero energy.

On the other hand, J_2 corresponds to the in-plane exchange coupling between two halogens from the same atomic plane, see Fig. 6a. In this case, the direct exchange interaction between the anion p-orbitals is weaker since the in-plane halogen-halogen distance is larger. Consequently, the indirect exchange interaction, involving the coupling between the halogen-p orbitals with the metal orbitals, should also play an important role in the next-nearest neighbor interaction. Group IIA and IIB metals are transferring their two outmost valence electrons to the halogens p-orbitals, to form the dihalide compounds. In the indirect exchange mechanisms, it is assumed that some covalent mixing between the cation and anion orbitals is energetically favorable. From the projected electronic density of states (PDOS) of strontium and cadmium dihalides, shown in Fig. 5b, one can indeed visualize the possible hybridization between the (spin-down) p orbitals of the halogen and the (spin-down) p or d orbitals of the metals near the Fermi level; note that for group IIB metal dihalides, the degeneracy between the metal d orbitals is partially lifted by the distorted octahedral crystal field, resulting in the formation of e_1(d_{xz} and d_{yz}), e_2($d_{x^2-y^2}$ and d_{xy}) and a_1(d_{z^2}) states. Specifically, the in-plane halogen-p_x/p_y orbitals can couple to metal-p_x/p_y orbitals and halogen-p_z orbitals couple to metal-p_z orbitals for strontium halides. For cadmium dihalides, the halogen-p_x/p_y orbitals couple to metal-$d_{x^2-y^2}/d_{xy}$ and d_{xz}/d_{yz} orbitals, and the halogen-p_z orbitals also hybridize with the d_{xz}/d_{yz} orbitals. From Table 1, J_2 of group IIA metal dihalides can be positive or

negative, indicating the competition between different indirect exchange mechanisms, such as the super-exchange coupling between orbitals pointing in the same direction (antiferromagnetic, e.g., hybridization between halogen-p_z orbitals with metal-p_z orbitals, as illustrated in Fig. 6c), the super-exchange mechanism involving the coupling between orthogonal orbitals (ferromagnetic, e.g., hybridization between halogen-p_x/p_y orbitals with metal-p_x/p_y orbitals, as depicted in Fig. 6c) and the double exchange mechanism (ferromagnetic). This latter mechanism involves the interaction between anions orbitals with different charged (or valence) states, e.g., between partially filled halogen orbitals (where holes are localized) with filled halogen orbitals. Very interestingly, J_2 is found to be positive for all group IIB metal halides (see Table 1), the coupling between the halogen p orbitals with the metal e_1 and e_2 states most likely favoring the ferromagnetic exchange mechanisms, as shown in Fig. 6d–f; note that the contribution of the metal d-states to the spin density, observed on Fig. 5a, also points towards the possible hybridization between the cation and anion orbitals near the Fermi level. Although GGA functional tends to over-delocalize electrons, the contribution of the metal d-states in CdBr$_2$ can still be confirmed in the spin density obtained from HSE06 functional.

We now consider the possible magnetic exchange interactions in planar 2DHDFM, namely without out-of-plane anion interactions. Similar to the case of P3m1-dihalides, J_1 of the P4/mmm-lithium monohalides decreases from LiCl to LiI, as can be seen in
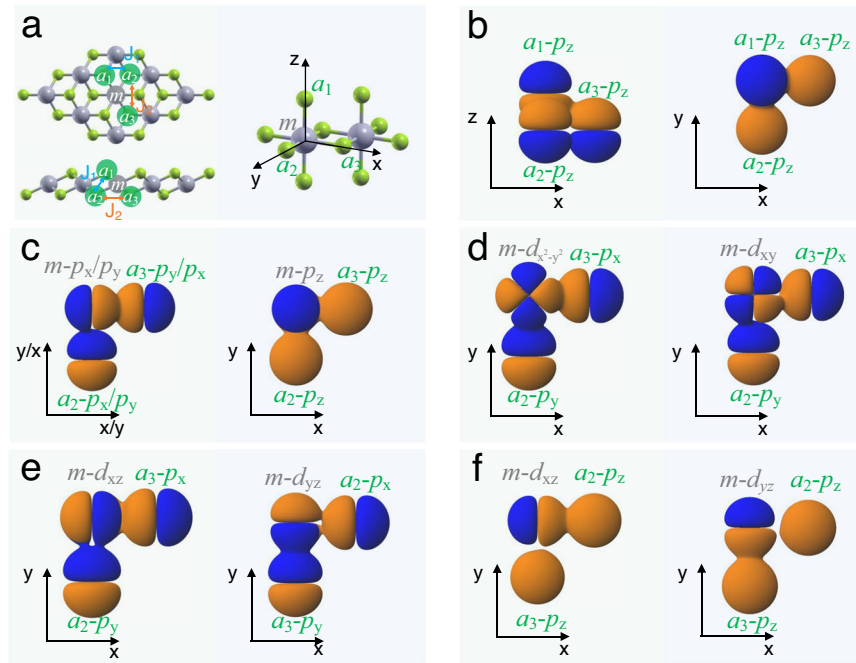
Fig. 6 Schematic diagram of the magnetic exchange interactions. a Exchange interaction paths in P3m1 metal dihalides. J_1 is the exchange coupling parameter originated from the halide ions on the upper layer (a_1) and the bottom layer (a_2). J_2 is the exchange coupling parameter originated from the halide ions on the same atomic plane (a_2 and a_3), m is the metal ions. Edge-sharing distorted ma_6 octahedra with the local xyz coordinates of the P3m1 structure are also given on the right. Schematic diagrams of (**b**) direct exchange between halogen-p_z orbitals, (**c**) the super-exchange interactions between halogen-p_x/p_y orbitals with metal-p_x/p_y orbitals and halogen-p_z orbitals with metal-p_z orbitals, (**d**) halogen-p_x/p_y orbitals with metal-$d_{x^2-y^2}/d_{xy}$ orbitals, (**e**) halogen-p_x/p_y orbitals with metal-d_{xz}/d_{yz} orbitals, and (**f**) halogen-p_z orbitals with metal-d_{xz}/d_{yz} orbitals.

Supplementary Table 1. In this case, as shown in Supplementary Fig. 2, J_1 is mainly due to the direct exchange between the halogen p_z-orbitals. In addition, from the PDOS shown in Supplementary Fig. 3, one can see that there is a very limited possible hybridization between the Li-s orbitals with the halogen-p orbitals, pointing out to a relatively weak indirect exchange interaction in these materials. On the other hand, in the case of hole-doped 2D planar P6m2-sulfides (such as ZnS and CdS) and nitrides (such as AlN and GaN), the ferromagnetic order is essentially mediated by the indirect exchange interaction between the sulfur or nitrogen p_z-states and the metal-d_{xz}/d_{yz} and p_z states, as evidenced by the PDOS in Supplementary Fig. 3.

Considering the possible use of these 2DHDFM in spintronic devices, the metal dihalides (like BaF$_2$ and CdF$_2$) appear as interesting candidates for high-temperature (above room temperature) applications. However, these materials might have some stability issues, possibly interacting/reacting with the ambient and being oxidized in air. On the other hand, potential more stable 2DHDFM have also been identified for low temperature applications. For example, AlN, GaN and ZnS crystallizes in the Wurtzite phase. In ultra-thin films (and at the 2D limit), such materials could be grown in a h-BN like phase[54–56]. In addition, these 2D materials should be much less reactive with the ambient. Other materials of interest are e.g., 2D ZrO$_2$ and TiO$_2$, which are predicted to be 2DHDFM with moderate Curie temperatures of 176 and 228 K, respectively.

In summary, using high-throughput density functional theory calculations, we have identified 122 stable 2DHDFM that exhibit a non-magnetic to a ferromagnetic phase transition upon hole doping. In these 2DHDFM, metal halides take up the biggest proportion, followed by the sulfides, oxides and nitrides. The magnetic properties of these 2D materials, such as their spin polarization energy, magnetic anisotropic energy, magnetic exchange coupling parameters and Curie temperature typically increase with the hole doping density. Among these materials, metal dihalides with a P3m1 phase, like BaF$_2$, CdF$_2$, PbCl$_2$ and PbBr$_2$ are predicted to have Curie temperatures above 300 K at a typical hole density of 6×10^{14} cm^{-2}, these materials being potentially interesting for spintronic devices operating above room temperature. In general, the ferromagnetic interaction in these materials is mediated by a direct exchange interaction between p_z-orbitals of anions in different atomic planes (out-of-plane coupling) as well as the indirect exchange interaction between the p_z-anion states and the metal p or d states (in-plane coupling). On the other hand, 2D planar materials with moderate Curie temperatures, typically ranging between 110 K and 230 K, have also been identified for possible spintronic applications at low temperature. Such materials are e.g., P6m2 sulfides and nitrides, like ZnS, AlN, and GaN. In these materials, the ferromagnetic coupling mainly arises from the indirect exchange interaction between the anion p_i-orbitals and the p or d metal states. These materials should be more stable than their halogen counterparts, especially considering their possible interaction with the ambient (oxidation), and could potentially be grown in a planar 2D form, like h-BN.

METHODS

In this work, all the density functional theory calculations were performed using the Vienna ab initio simulation package (VASP) package[57,58], with electron-ion interaction described by projector augmented wave (PAW) pseudopotentials. The generalized gradient approximation (GGA), parameterized by the Perdew-Burke-Ernzerhof (PBE)[59] approach was used as the exchange correlation functional. The energy cutoff of 550 eV and k-point meshes of $0.03 \times 2\pi$ and $0.02 \times 2\pi$ Å^{-1} were used for structural optimizations and self-consistent calculations. Total energy convergence criterion of 10^{-6} eV per cell and force convergence

criterion of 0.005 eV Å^{-1} were chosen for complete relaxations of lattice constants as well as atomic positions. The Heyd−Scuseria−Ernzerhof functional (HSE06)[60], which mixes 25% nonlocal exchange with the PBE functional, was also used for testing purpose. In the doping calculations, the hole density was tuned by removing electrons from the cell, with a jellium background with opposite charge added to maintain charge neutrality and the atomic positions are reoptimized at different hole densities. This method has been used to obtain the spin polarization energies for various systems under hole doping.

Phonon dispersion curves were calculated by the PHONOPY package[61] on the basis of Density Functional Perturbation Theory (DFPT). Curie temperatures were estimated using Monte Carlo simulations, as implemented in the VAMPIRE package[62]. The simulated systems for all materials consist of a platelet with at least 10,000 spins with a rectangular supercell. The spins were thermalized for 10,000 equilibrium steps, followed by 20,000 averaging steps for the calculation of the thermal equilibrium magnetization at every temperature.

The ab initio evolutionary algorithm was performed by USPEX[49,63], interfaced with VASP, was used to find the potential structures that are ferromagnetic under hole doping. The variable-composition searching was chosen with the total atom numbers of the 2D crystals set to be 2–8, and their thicknesses and vacuum spaces restricted to be 4 Å and 20 Å, respectively. 150 groups of symmetry were used to produce random symmetric structure generator for initial population. Then, the full structure relaxations were performed, and the most stable and metastable structures were screened and inherited into the next generation by comparing their formation enthalpy. The number of generations is set to 40.

DATA AVAILABILITY
The data that support the findings of this study are available from the corresponding authors on reasonable request.

CODE AVAILABILITY
The codes used to carry out this work are described and referenced in the Methods section and are available free-of-charge with the exception of VASP.

REFERENCES
1. Wolf, S. et al. Spintronics: a spin-based electronics vision for the future. *Science* **294**, 1488–1495 (2001).
2. Žutić, I., Fabian, J. & Sarma, S. D. Spintronics: fundamentals and applications. *Rev. Mod. Phys.* **76**, 323 (2004).
3. Bader, S. & Parkin, S. Spintronics. *Annu. Rev. Condens. Matter Phys.* **1**, 71–88 (2010).
4. Dietl, T. A ten-year perspective on dilute magnetic semiconductors and oxides. *Nat. Mater.* **9**, 965–974 (2010).
5. Dietl, T. & Ohno, H. Dilute ferromagnetic semiconductors: physics and spintronic structures. *Rev. Mod. Phys.* **86**, 187 (2014).
6. Dietl, T., Ohno, H., Matsukura, F., Cibert, J. & Ferrand, D. Zener model description of ferromagnetism in zinc-blende magnetic semiconductors. *Science* **287**, 1019–1022 (2000).
7. Coey, J. d^0 ferromagnetism. *Solid State Sci.* **7**, 660–667 (2005).
8. Zhou, S. et al. Room temperature ferromagnetism in carbon-implanted ZnO. *Appl. Phys. Lett.* **93**, 232507 (2008).
9. Herng, T. S. et al. Room-temperature ferromagnetism of Cu-doped ZnO films probed by soft X-ray magnetic circular dichroism. *Phys. Rev. Lett.* **105**, 207201 (2010).
10. Yi, J. et al. Ferromagnetism in dilute magnetic semiconductors through defect engineering: Li-doped ZnO. *Phys. Rev. Lett.* **104**, 137201 (2010).
11. Pan, H. et al. Room-temperature ferromagnetism in carbon-doped ZnO. *Phys. Rev. Lett.* **99**, 127201 (2007).
12. Peng, H., Li, J., Li, S.-S. & Xia, J.-B. Possible origin of ferromagnetism in undoped anatase TiO$_2$. *Phys. Rev. B* **79**, 092411 (2009).
13. Dev, P., Xue, Y. & Zhang, P. Defect-induced intrinsic magnetism in wide-gap III nitrides. *Phys. Rev. Lett.* **100**, 117204 (2008).
14. Peng, H. et al. Origin and enhancement of hole-induced ferromagnetism in first-row d^0 semiconductors. *Phys. Rev. Lett.* **102**, 017201 (2009).
15. Gibertini, M., Koperski, M., Morpurgo, A. F. & Novoselov, K. S. Magnetic 2D materials and heterostructures. *Nat. Nanotechnol.* **14**, 408–419 (2019).
16. Molle, A. et al. Buckled two-dimensional Xene sheets. *Nat. Mater.* **16**, 163–169 (2017).
17. Gong, C. & Zhang, X. Two-dimensional magnetic crystals and emergent hetero-structure devices. *Science* **363**, 6428 (2019).
18. Jiang, X. et al. Recent progress on 2D magnets: Fundamental mechanism, structural design and modification. *Appl. Phys. Rev.* **8**, 031305 (2021).
19. Huang, B. et al. Layer-dependent ferromagnetism in a van der Waals crystal down to the monolayer limit. *Nature* **546**, 270–273 (2017).
20. Gong, C. et al. Discovery of intrinsic ferromagnetism in two-dimensional van der Waals crystals. *Nature* **546**, 265–269 (2017).
21. Deng, Y. et al. Gate-tunable room-temperature ferromagnetism in two-dimensional Fe$_3$GeTe$_2$. *Nature* **563**, 94–99 (2018).
22. Bonilla, M. et al. Strong room-temperature ferromagnetism in VSe$_2$ monolayers on van der Waals substrates. *Nat. Nanotechnol.* **13**, 289–293 (2018).
23. Tiwari, S., Van de Put, M. L., Sorée, B. & Vandenberghe, W. G. Critical behavior of the ferromagnets CrI$_3$, CrBr$_3$, and CrGeTe$_3$ and the antiferromagnet FeCl$_2$: a detailed first-principles study. *Phys. Rev. B* **103**, 014432 (2021).
24. Zhang, L., Zhou, J., Li, H., Shen, L. & Feng, Y. P. Recent progress and challenges in magnetic tunnel junctions with 2D materials for spintronic applications. *Appl. Phys. Rev.* **8**, 021308 (2021).
25. Feng, Y. P. et al. Prospects of spintronics based on 2D materials. *Wiley Interdiscip. Rev.: Comput. Mol. Sci.* **7**, e1313 (2017).
26. Song, T. et al. Giant tunneling magnetoresistance in spin-filter van der Waals heterostructures. *Science* **360**, 1214–1218 (2018).
27. Tiwari, S., Van de Put, M. L., Sorée, B. & Vandenberghe, W. G. Magnetic order and critical temperature of substitutionally doped transition metal dichalcogenide monolayers. *npj 2D Mater. Appl.* **5**, 1–7 (2021).
28. Ramasubramaniam, A. & Naveh, D. Mn-doped monolayer MoS$_2$: An atomically thin dilute magnetic semiconductor. *Phys. Rev. B* **87**, 195201 (2013).
29. Yun, S. J. et al. Ferromagnetic order at room temperature in monolayer WSe$_2$ semiconductor via vanadium dopant. *Adv. Sci.* **7**, 1903076 (2020).
30. Yang, L. et al. Ta doping enhanced room-temperature ferromagnetism in 2D semiconducting MoTe$_2$ nanosheets. *Adv. Electron. Mater.* **5**, 1900552 (2019).
31. Wu S, et al. Magnetism in p-type monolayer gallium chalcogenides (GaSe, GaS). Preprint at https://arxiv.org/abs/1409.4733 (2014).
32. Cao, T., Li, Z. & Louie, S. G. Tunable magnetism and half-metallicity in hole-doped monolayer GaSe. *Phys. Rev. Lett.* **114**, 236602 (2015).
33. Meng, R. et al. Two-dimensional gallium and indium oxides from global structure searching: ferromagnetism and half metallicity via hole doping. *J. Appl. Phys.* **128**, 034304 (2020).
34. Meng, R. et al. Ferromagnetism and half-metallicity in two-dimensional MO (M=Ga,In) monolayers induced by hole doping. *Phys. Rev. Mater.* **4**, 074001 (2020).
35. Iordanidou, K. et al. Hole-doped 2D InSe for spintronic applications. *ACS Appl. Nano Mater.* **1**, 6656–6665 (2018).
36. Houssa, M., Iordanidou, K., Pourtois, G., Afanasiev, V. & Stesmans, A. Ferro-magnetism in two-dimensional hole-doped SnO. *AIP Adv.* **8**, 055010 (2018).
37. Seixas, L., Rodin, A. S., Carvalho, A. & Castro Neto, A. H. Multiferroic two-dimensional materials. *Phys. Rev. Lett.* **116**, 206803 (2016).
38. Wang, Y. et al. Lead monoxide: a two-dimensional ferromagnetic semiconductor induced by hole-doping. *J. Mater. Chem. C* **5**, 4520–4525 (2017).
39. Miao, N., Xu, B., Bristowe, N. C., Zhou, J. & Sun, Z. Tunable magnetism and extraordinary sunlight absorbance in indium triphosphide monolayer. *J. Am. Chem. Soc.* **139**, 11125–11131 (2017).
40. Nie, Y. et al. Room-temperature half-metallicity in monolayer honeycomb structures of group-V binary compounds with carrier doping. *Phys. Rev. B* **96**, 075401 (2017).
41. Zhang, C., Liu, J., Shen, H., Li, X. & Sun, Q. Identifying the ground state geometry of a MoN$_2$ sheet through a global structure search and its tunable p-electron half-metallicity. *Chem. Mater.* **29**, 8588–8593 (2017).
42. Wu, C.-W. & Yao, D.-X. Robust p-orbital half-metallicity and high Curie-temperature in the hole-doped anisotropic TcX$_2$ (X=S,Se) nanosheets. *J. Magn. Magn. Mater.* **478**, 68–76 (2019).
43. Zhang, Y., Oka, T., Suzuki, R., Ye, J. & Iwasa, Y. Electrically switchable chiral light-emitting transistor. *Science* **344**, 725–728 (2014).
44. Ye, J. et al. Liquid-gated interface superconductivity on an atomically flat film. *Nat. Mater.* **9**, 125–128 (2010).

45. Efetov, D. K. & Kim, P. Controlling electron-phonon interactions in graphene at ultrahigh carrier densities. *Phys. Rev. Lett.* **105**, 256805 (2010).

46. Haastrup, S. et al. The Computational 2D Materials Database: high-throughput modeling and discovery of atomically thin crystals. *2D Mater.* **5**, 042002 (2018).

47. Mounet, N. et al. Two-dimensional materials from high-throughput computational exfoliation of experimentally known compounds. *Nat. Nanotechnol.* **13**, 246–252 (2018).

48. Zhou, J. et al. 2DMatPedia, an open computational database of two-dimensional materials from top-down and bottom-up approaches. *Sci. Data* **6**, 1–10 (2019).

49. Lyakhov, A. O., Oganov, A. R., Stokes, H. T. & Zhu, Q. New developments in evolutionary structure prediction algorithm USPEX. *Comput. Phys. Commun.* **184**, 1172–1182 (2013).

50. Sivadas, N., Daniels, M. W., Swendsen, R. H., Okamoto, S. & Xiao, D. Magnetic ground state of semiconducting transition-metal trichalcogenide monolayers. *Phys. Rev. B* **91**, 235425 (2015).

51. Fuh, H. R. et al. Newtype single-layer magnetic semiconductor in transition-metal dichalcogenides VX_2 (X = S, Se and Te). *Sci. Rep.* **6**, 32625 (2016).

52. Tiwari, S., Vanherck, J., Van de Put, M. L., Vandenberghe, W. G. & Sorée, B. Computing Curie temperature of two-dimensional ferromagnets in the presence of exchange anisotropy. *Phys. Rev. Res.* **3**, 043024 (2021).

53. Lado, J. L. & Fernández-Rossier, J. On the origin of magnetic anisotropy in two dimensional CrI_3. *2D Mater.* **4**, 035002 (2017).

54. Freeman, C. L., Claeyssens, F., Allan, N. L. & Harding, J. H. Graphitic nanofilms as precursors to wurtzite films: theory. *Phys. Rev. Lett.* **96**, 066102 (2006).

55. Tusche, C., Meyerheim, H. & Kirschner, J. Observation of depolarized ZnO (0001) monolayers: formation of unreconstructed planar sheets. *Phys. Rev. Lett.* **99**, 026102 (2007).

56. Tsipas, P. et al. Evidence for graphite-like hexagonal AlN nanosheets epitaxially grown on single crystal Ag (111). *Appl. Phys. Lett.* **103**, 251605 (2013).

57. Kresse, G. From ultrasoft pseudopotentials to the projector augmented-wave method. *Phys. Rev. B* **59**, 1758–1775 (1999).

58. Kresse, G. & Furthmüller, J. Efficient iterative schemes for ab initio total-energy calculations using a plane-wave basis set. *Phys. Rev. B* **54**, 11169 (1996).

59. Perdew, J. P., Burke, K. & Ernzerhof, M. Generalized gradient approximation made simple. *Phys. Rev. Lett.* **77**, 3865 (1996).

60. Heyd, J., Scuseria, G. E. & Ernzerhof, M. Hybrid functionals based on a screened Coulomb potential. *J. Chem. Phys.* **118**, 8207–8215 (2003).

61. Togo, A. & Tanaka, I. First principles phonon calculations in materials science. *Scr. Mater.* **108**, 1–5 (2015).

62. Evans, R. F. et al. Atomistic spin model simulations of magnetic nanomaterials. *J. Phys.: Condens. Matter* **26**, 103202 (2014).

63. Oganov, A. R. & Glass, C. W. Crystal structure prediction using ab initio evolutionary techniques: principles and applications. *J. Chem. Phys.* **124**, 244704 (2006).

ACKNOWLEDGEMENTS

AUTHOR CONTRIBUTIONS

R.M. and M.H. conceptualized the work. R.M. was responsible for all the calculations. The manuscript was written by R.M. and M.H. All authors contributed to the discussions and analyses of the data and approved the final version.

COMPETING INTERESTS

The authors declare no competing interests.

ADDITIONAL INFORMATION

Supplementary information The online version contains supplementary material available at https://doi.org/10.1038/s41524-022-00916-2.

Correspondence and requests for materials should be addressed to Ruishen Meng or Michel Houssa.

Reprints and permission information is available at http://www.nature.com/reprints

Publisher's note Springer Nature remains neutral with regard to jurisdictional claims in published maps and institutional affiliations.